Mutual Interaction Noise in Rotor-Beam Configuration

Emma Vella, Romain Gojon, Helene Parisot-Dupuis, Nicolas Doué, Thierry Jardin, Michel Roger

10.2514/6.2024-3318

Mutual Interaction Noise in Rotor-Beam Configuration

Emma Vella*, Romain Gojon†, Hélène Parisot-Dupuis‡, Nicolas Doué§ and Thierry Jardin¶
ISAE-SUPAERO, Université de Toulouse, Toulouse, France

Michel Roger‖
Ecole Centrale de Lyon, Ecully, 69134, France

In small-size UAVs configurations, rotor-beam interaction noise is an important contributor to the tonal noise. With the beam located in the close wake of the rotor, distinct and coupled noise source mechanisms can occur. Both rotor blades and beam radiate sound as both experience unsteady loading due to the presence of each other. The former can be described by a blade-potential interaction noise model; i.e. blades undergo a potential distortion when passing close to the cylindrical beam. Similarly, the latter arises from potential interaction between the blade and the beam; i.e. the beam experiences variation in incoming flow speed and loading when the blade passes above it. In this paper, we combine those models to predict the noise radiated by a rotor-beam configuration and compare our results with experimental and numerical results from previous studies.

I. Nomenclature

B	=	number of rotor blades
BPF	=	blade passing frequency [Hz]
c_0	=	speed of sound [m/s]
c	=	airfoil chord [m]
$C(x)$	=	Theodorsen function
D_b	=	beam diameter [m]
D	=	rotor diameter [m]
FWH	=	Ffowcs-Williams and Hawkings
$iLES$	=	incompressible large eddy scale simulation
J_n	=	Bessel function
k	=	loading harmonic
k_{mB}	=	$mB\Omega/c_0$, wavenumber related to the blade passing frequency
L	=	rotor-beam separation distance [m]
m	=	sound harmonic
PIV	=	particle image velocimetry
(r, ϕ)	=	polar coordinates
r_{root}	=	root radius [m]
r_{tip}	=	tip radius [m]
R	=	observer distance from the rotor center [m]
RPM	=	rotation per minute [min^{-1}]
SPL	=	sound pressure level [dB]
t	=	time [s]
U_z	=	rotor induced velocity [m/s]
U_r	=	velocity at the blade section r [m/s]
UAV	=	unmanned air vehicles

*Research Engineer, ISAE-SUPAERO, Toulouse, France, emma.vella@isae-supaero.fr.
†Associate Professor, ISAE-SUPAERO, Toulouse, France, romain.gojon@isae-supaero.fr, AIAA Member.
‡Associate Professor, ISAE-SUPAERO, Toulouse, France, helene.parisot-dupuis@isae-supaero.fr, AIAA Member.
§Associate Professor, ISAE-SUPAERO, Toulouse, France, nicolas.doue@isae-supaero.fr.
¶Research Associate, ISAE-SUPAERO, Toulouse, France, thierry.jardin@isae-supaero.fr.
‖Professor, Laboratoire de Mécanique des Fluides et Acoustique, michel.roger@ec-lyon.fr.

γ = blade stagger angle with respect to the rotor axis [°]
α = blade pitch angle [°]
α_0 = flow swirl angle [°]
Ω = rotor angular speed [rad/s]
ϕ_{exp} = azimuth observer position considered in the experiments [°]
Φ = azimuth observer position considered in the model [°]
θ_{exp} = latitude observer position considered in the experiments [°]
Θ = latitude observer position considered in the model [°]
ρ_0 = air ambient density

II. Introduction

Unmanned air vehicles (UAVs) operate over a wide range of missions, in both urban and military environments. In civilian environments, UAVs contribute to noise pollution and may be a concern for public health in a near future. Among small-size UAVs used in this context, multicopters are one of the most widespread solution because of their inherent stability, agility and versatility. Yet, in addition to rotor self-noise, multicopters are characterized by noise due to interactions between rotors and airframes, among which rotor-beam interactions are an important contributor to the acoustic footprint. Specifically, it can be easily understood that rotor-beam interactions are an important contributor to tonal noise at the blade passing frequency (BPF) and its harmonics since interactions occur each time blades pass near the beam.

A few studies have addressed this topic of UAV rotors operating at low Mach and low Reynolds numbers and interacting with a beam. Looking first at experimental and numerical studies, Zawodny and Boyd [1] showed good agreement between experimental and numerical results for the case of a cylindrical beam placed in the wake of the rotor. For a microphone located at a latitude angle of $-45°$ and in a plane orthogonal to the beam (at an azimuth angle of 90°), the authors showed that the magnitude of BPF harmonics can be greater than that of the BPF. Furthermore, they found that noise contribution from the beam may be dominant at this microphone location, when compared to another microphone located at an azimuth angle of 0° aligned with the beam. This was further discussed by Gojon et al. [2] who reported directivities of the first BPF harmonics over a wide range of azimuth and latitude angles. In a more recent paper, Gojon et al. [3] provided the community with an experimental, open database of low Reynolds number rotors in interaction with beams of different shapes. The envelope of BPF harmonics was characterized by two humps, a first one centered around 5×BPF and a second one centered around 20×BPF-25×BPF. Focusing on the first hump, the main outcomes of this parametric study were that the magnitude of the first BPF harmonics increased with beam diameter, rotational speed and number of blades but decreased with rotor-beam separation distance. Later Doué et al. [4] obtained numerical results (with incompressible implicit large eddy simulations in combination with a solid Ffowcs Williams and Hawkings (FWH) formulation) and, by isolating the contributions from the rotor on the one hand and from the beam on the other hand, demonstrated that amplitudes of BPF harmonics of the first hump are mainly due to the beam radiation. Moreover, the authors applied a solid FWH formulation on 13 sections of the beam. The distribution of acoustic sources along the beam showed that maximum magnitudes of 5×BPF, 7×BPF and 9×BPF harmonics were located between $r = 0.8r_{tip}$ and $0.9r_{tip}$. A few investigations were carried out on the aerodynamics of tip-vortices impinging on a beam. Measurements of wall-pressure on a cylindrical beam downstream the rotor were analyzed by Brand et al. [5] within the framework of helicopter rotor and tail interaction. For almost the same configuration, a few years later, results from a numerical approach were compared to experimental measurements by Affes et al. [6], [7].

Other works have addressed rotor-beam interaction noise theoretically. For example, Roger et al. [8] derived an analytical model for the steady-loading and unsteady-loading noise of rotor blades, due to blade-potential interaction. Contribution from the beam was added using a cylinder-scattering model, which was justified by the fact that the experimental setup they modeled was very compact. Analytical models of steady and unsteady loading noise from rotor blades and beam were also derived by Wu et al. [9]. The authors obtained analytical results in good agreement with experimental and numerical acoustic pressure signals (same directivity behaviors regarding rotor and beam contributions were found), although the analytical model slightly overestimated the amplitude of pressure impulse in the farfield. Despite these few studies, there is a general lack of theoretical works on rotor-beam interaction noise and assessment of analytical models against numerical and experimental data. Yet, these models provide an efficient tool for the analysis of the physics involved in such configurations.

This paper presents the analytical modeling of the tonal noise generated by small low Reynolds number rotors in interaction with beams of circular cross-section. Two analytical models are first outlined, considering uncoupled noise

generation mechanisms : the blade-potential interaction noise model and the beam-potential interaction noise model, related to the unsteady loading on the rotor blades and the beam. They are then compared to experimental and numerical results from Gojon et al. [2].

III. Rotor-Beam Configuration

A. Noise Generation Mechanisms

The rotor-beam configuration presented in the following includes a small UAV two-bladed rotor and a cylindrical beam of circular cross-section downstream of the rotor, both supported on a cylindrical mast (Fig. 1). In this configuration, various aeroacoustic mechanisms are involved :

1) The thickness noise, which is caused by the displacement of air due to the moving blades. This is strongly dependant on the blade thickness as it is a key parameter to determine the volume of fluid displaced;
2) The blade loading noise, corresponding to the accelerated force $\boldsymbol{F}_{blade}(r, \phi)$ generated by moving blade surface. This loading can be steady, i.e. no load fluctuations occur along the azimuthal direction. The steady loading is dependant on the rotor aerodynamic characteristics only : the thrust and the torque. The loading can also be unsteady. In our case the loading fluctuations are caused by a stationary azimuthal flow distortion due to the presence of the beam;
3) The unsteady beam loading noise, which can be caused by various unsteady aerodynamic effects such as blades circulation nearby or wake and tip-vortex impingement on the beam. Steady loading on the beam does not contribute to the sound, since the beam is motionless.
4) And finally the scattering of sound by the blades and the beam. Acoustic waves from sources located on the rotor can be diffracted by the beam and conversely, acoustic waves from the beam can be diffracted by the rotor blades. Evanescent acoustic waves may become efficient in the farfield through diffraction by the beam or the rotor blades.

As small UAV rotors are characterized by low Mach numbers, the noise contribution from quadripolar sources due to the turbulence in rotor wakes is neglected here.

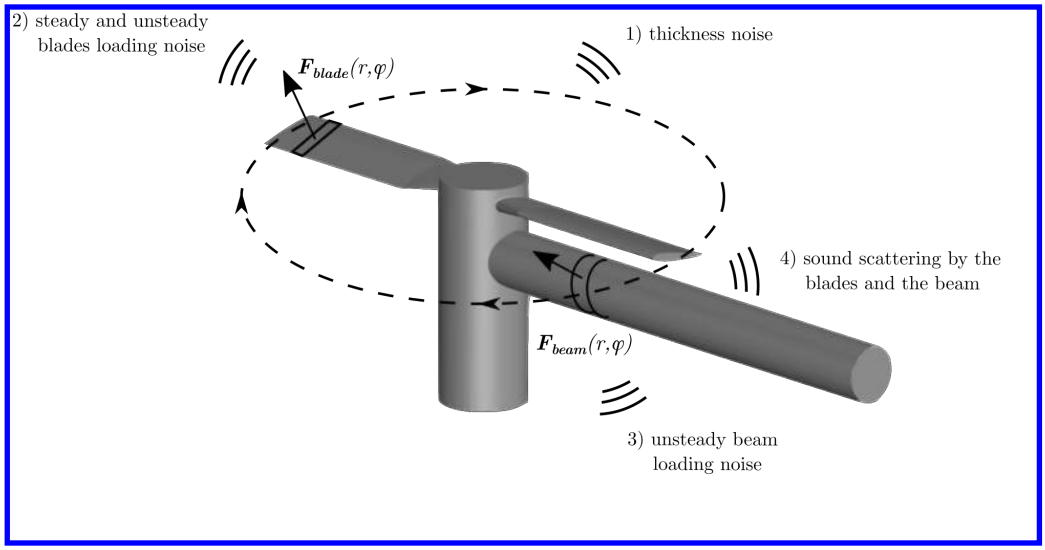

Fig. 1 Aeroacoustic mechanisms involved in rotor-beam configuration.

In the following analytical modeling, only two of these aeroacoustic mechanisms will be described in detail. The first one is the noise generated by the unsteady loading on the blades due to the presence of the cylindrical beam, corresponding to the source term described in 2). The second one is the noise generated by the unsteady loading on the beam due to the blades circulation nearby, corresponding to the source term described in 3).

B. Experimental Setup

For experimental investigation, the rotor-beam arrangement is placed at the center of the ISAE SUPAERO anechoic room. The arc antenna of microphones is used to measure the farfield noise radiated at $R = 1.62$ m away from the rotor center, for latitude angles θ_{exp} every 10° from −60° to +60°, where 0° corresponds to the rotor disk plane. The distance of 1.62 m from the rotor center to the microphone of the arc antenna is assumed in the geometric farfield. The support mast is fixed on a turntable so that the rotor-beam arrangement can rotate around the z axis. The farfield noise can thus be measured for various azimuth angle ϕ_{exp} in order to obtain almost three dimensional noise directivities. The azimuth angle $\phi_{exp} = 0°$ is defined for the setup position showed in Fig. 2, i.e. the arc antenna of microphones is placed opposite to the beam. The observer position is thus defined by $(R, \theta_{exp}, \phi_{exp})$ for experiments. The full experimental setup is described by Gojon et al. [3]. All the geometric and aerodynamic parameters are detailed in IV.C.

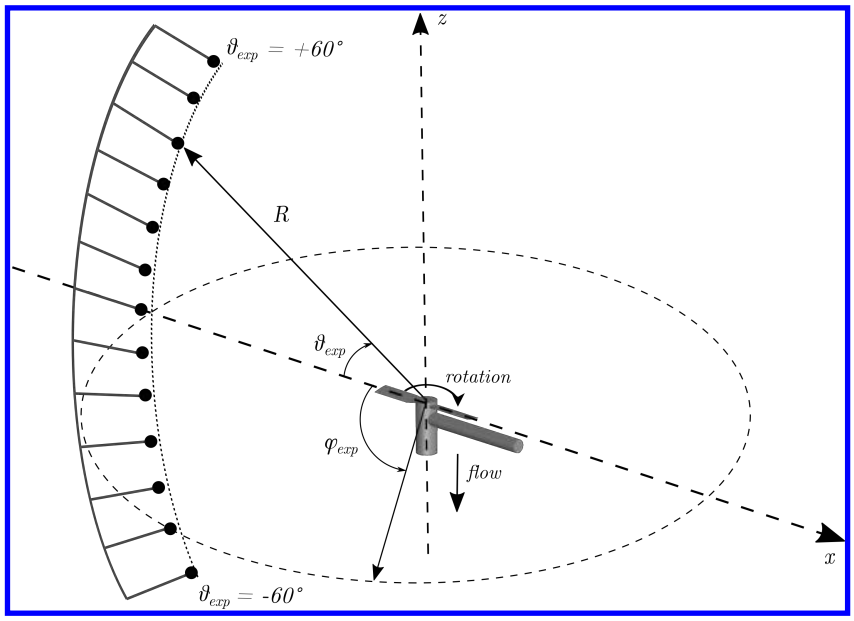

Fig. 2 Schematic of the experimental setup. The arc antenna of microphones is fixed and the support mast can be rotated around the z axis. Not to scale.

IV. Analytical Modeling

A. Blade Potential-Interaction Noise

The tonal noise generated in the farfield, at the m^{th} harmonic of the BPF, by rotor blades experiencing a stationary distortion induced by the presence of the beam is calculated in this section. The model is based on Hanson's work on noise of rotors [10]. Specifically, Hanson's model is used considering hovering conditions (i.e. the Doppler factor associated with advance ratio is unity) and assuming that the radial loading is negligible :

$$p_{mB}(\mathbf{x},t) = \frac{-ik_{mB}B}{4\pi R}\sum_{k} e^{i[(mB-k)(\Phi-\frac{\pi}{2})+mB\Omega(\frac{R}{c_0}-t)]} \int_{root}^{tip} J_{mB-k}\left(mB\frac{\Omega r}{c_0}\sin(\Theta)\right)\left[\frac{mB-k}{rk_{mB}}F^{(k)}_{blade,\phi}(r)+\cos(\Theta)F^{(k)}_{blade,z}(r)\right]dr\,, \tag{1}$$

with $(R, \Theta, \Phi) = (R, \pi/2 - \theta_{exp}, \pi - \phi_{exp})$ the observer position. $F^{(k)}_{blade,z}$ and $F^{(k)}_{blade,\phi}$ are the k^{th} harmonics of the axial and tangential forces, respectively. Steady loading noise is related to the steady part of these forces, $F^{(0)}_{blade,z}$ and $F^{(0)}_{blade,\phi}$, and higher loading harmonics k are related to the unsteady part. Integration is performed over the blade radius only, the chord being considered acoustically compact in the present case. This approximation is reasonable up to

$f = 1400$ Hz, i.e. up to 6×BPF. The k^{th} harmonics of the axial and tangential forces read :

$$F^{(k)}_{blade,z}(r) = -L_k(r)\sin\gamma \quad , \quad F^{(k)}_{blade,\phi}(r) = L_k(r)\cos\gamma\,, \tag{2}$$

with γ the blade stagger angle with respect to the rotor axis and L_k denoting the harmonics of lift per unit span:

$$\begin{aligned} L_k(r) &= \pi\rho_0 c U_r w_k(r)\overline{\left[C(\sigma)(J_0(\mu) - iJ_1(\mu)) + \frac{i\sigma}{\mu}J_1(\mu)\right]}, \\ \sigma &= \frac{k\Omega c}{2U_r} \quad ; \quad \mu = \frac{ikc}{2r}e^{-i\gamma}\,, \end{aligned} \tag{3}$$

with the overbar indicating the complex conjugate. These harmonics L_k are derived from Sears' theory [11]. They are produced by a stationnary azimuthal flow distortion induced by the presence of the beam located in the wake of the rotor. Specifically, the distortion is modelled as an azimuthal variation of the velocity induced as a reaction to rotor thrust and torque generation, i.e. downwash and swirl, respectively. That is, the induced velocity seen by the blades is reduced in the vicinity of the beam. This reduction in downward and tangential velocity can be viewed as an 'upwash' relative to the induced velocity in the absence of the beam and we hence refer to it as 'upwash' in what follows. The upwash velocity normal to the chord, involved in Sears' theory, can be obtained from the solution of the incompressible potential flow problem around a circle presented in Fig. 3. In this equivalent problem, at a given section r, the rotor blade is modeled as a two-dimensional flat plate with a velocity Ωr in the y-direction and the beam as a circle. $U_z(r)$ is the axial rotor-induced velocity at the section of radius r.

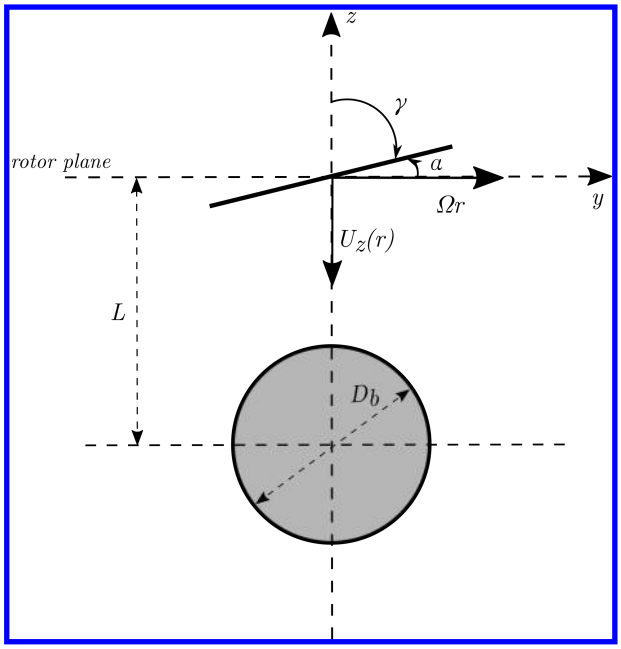

Fig. 3 Schematic of the equivalent two-dimensional incompressible blade-potential flow problem.

Roger et al. [12] derived the expression of the flow distortion in the direction parallel to the rotor axis u and in the tangential direction v as :

$$\begin{aligned} \frac{u(r,\phi)}{-U_z(r)(D_b/2)^2} &= A(r,\phi)\cos\alpha_0 + B(r,\phi)\sin\alpha_0, \\ \frac{v(r,\phi)}{-U_z(r)(D_b/2)^2} &= C(r,\phi)\sin\alpha_0 - D(r,\phi)\cos\alpha_0, \end{aligned} \tag{4}$$

with $A(r,\phi)$, $B(r,\phi)$, $C(r,\phi)$ and $D(r,\phi)$:

$$A(r,\phi) = \frac{L^2 - r^2\sin^2\phi}{[L^2 + r^2\sin^2\phi]^2} \quad , \quad B(r,\phi) = 2L\frac{r\sin\phi}{[L^2 + r^2\sin^2\phi]^2},$$
$$C(r,\phi) = \frac{\cos\phi(L^2 - r^2\sin^2\phi)}{[L^2 + r^2\sin^2\phi]^2} \quad , \quad D(r,\phi) = L\frac{r\sin 2\phi}{[L^2 + r^2\sin^2\phi]^2},$$

with α_0 denoting the flow swirl angle with the rotor axis and α being the blade pitch angle. The following expression of the upwash velocity w, i.e. in the direction normal to the chord, is written as a combination of velocity components u and v (4) and the pitch angle α:

$$\frac{w(r,\phi)}{U_z(r)(D_b/2)^2} = \begin{cases} \sin\alpha\sin\alpha_0\ C(r,\phi) - \sin\alpha\cos\alpha_0\ D(r,\phi) & \\ \qquad + \cos\alpha\cos\alpha_0\ A(r,\phi) + \cos\alpha\sin\alpha_0\ B(r,\phi), & \text{if } \phi \in [\frac{\pi}{2};\frac{3\pi}{2}] \\ 0 & \text{otherwise.} \end{cases} \tag{5}$$

Note that w is 0 outside $[\frac{\pi}{2};\frac{3\pi}{2}]$ since the cylindrical beam only extends on one half of the rotor disk plane (a blade experiences one distortion per rotation). Then, since the distortion experienced by the blades is periodic, it can be expanded as a Fourier series, leading to upwash harmonics w_k :

$$w_k(r) = \frac{1}{2\pi}\int_0^{2\pi} w(r,\phi)e^{ik\phi}d\phi, \quad k \geq 1. \tag{6}$$

A similar formula for the upwash harmonics is derived by Wu [9] using the method described by Parry [13] for the two-dimensional potential field around an ellipse positioned in a uniform flow. In this case no swirl angle is considered, meaning that the flow induced by the rotor is assumed to be parallel to the rotor axis:

$$w_k(r) = \frac{-ikU_z(r)D_b^2}{8r^2}e^{\frac{-k}{r}L+i\gamma}(-1)^k, \quad k \geq 1. \tag{7}$$

This latter formulation is used in what follows.

B. Beam Potential-Interaction Noise

The unsteady loading noise here arises from the cylindrical beam experiencing a gust each time a rotor blade passes nearby. Its farfield expression is based on Lowson's work on noise of rotor-stator stages in compressors [14]. The formula of the stator tonal noise at the m^{th} harmonic of the BPF is adapted for a beam, considered as equivalent to a stator with only one vane:

$$\begin{aligned} p_m(\mathbf{x},t) = \frac{-ik_{mB}}{4\pi R}\sum_k e^{i[(mB-k)(\Phi-\frac{\pi}{2})+mB\Omega(\frac{R}{c_0}-t)]} \\ \int_{root}^{tip} J_{mB-k}\left(mB\frac{\Omega r}{c_0}\sin(\Theta)\right)\left[\frac{mB-k}{rk_{mB}}F^{(m)}_{beam,\phi}(r) + \cos(\Theta)F^{(m)}_{beam,z}(r)\right]dr. \end{aligned} \tag{8}$$

This farfield noise formulation involves the same Bessel functions as the rotor noise equation (1), which defines similar radiation efficiency of the source terms. The first main difference is the missing term B in the expression of the noise radiated by the beam. The other main difference is that, in the case of the beam (8), each spatial harmonic of the rotor wake is transformed into a single temporal harmonic of the beam radiation. Only one loading harmonic contributes to each sound harmonic m since the beam is stationary. Other terms in equations (1) and (8) are exactly the same, stressing that beam noise and rotor noise are radiated at the same frequencies.

The modeling of loading fluctuations on the beam is suggested by Wu et al. [9] with a simple analytical model. This second model is obtained, as the first one, from the solution of an incompressible potential flow problem around a two-dimensional circular cylinder of diameter D_b (see Fig. 4). At a given section r, the rotor blade is modeled as a line vortex with circulation $\Gamma(r) > 0$. We need to account for a positive circulation for a counterclockwise rotation, since the vortex moves from left to right. The vortex is located at $X = X_v = \Omega rt$ (i.e. the vortex moves with a velocity Ωr in the X-direction) and $Y = Y_v = L$ with respect to the origin located on the cylinder axis. The vortex and the cylinder are placed in a flow of velocity $U_z(r)$ along the Y axis. As for the previous model, $U_z(r)$ corresponds to the axial rotor-induced velocity at the section r.

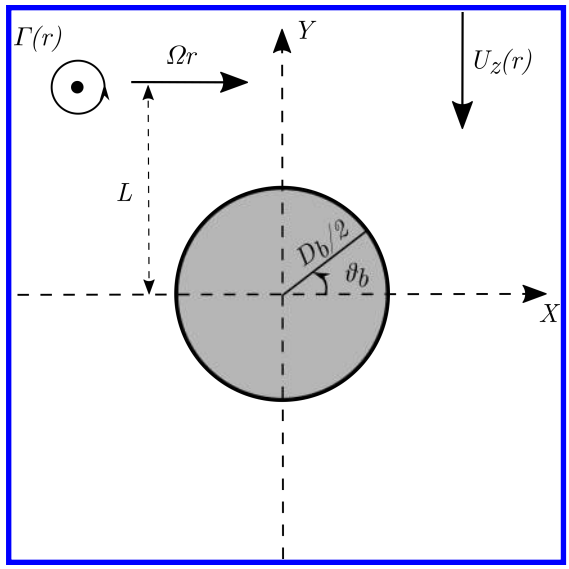

Fig. 4 Schematic of the equivalent two-dimensional incompressible beam-potential flow problem.

In order to solve this equivalent two-dimensional incompressible potential flow problem, a complex potential is introduced $f(Z) = \Phi(Z) + i\Psi(Z)$, with the complex coordinate $Z = X + iY$ and Φ and Ψ, respectively the velocity potential and the stream function. The complex potential produced by a vortex and a freestream flow reads :

$$f(Z) = -\frac{i\Gamma(r)}{2\pi} ln\Big(Z - Z_v\Big) + iU_z(r)Z. \tag{9}$$

Using Milne-Thompson's circle theorem, the circular cylinder contribution is added into the equation by considering a new complex potential flow $f(Z) + \overline{f(D_b^2/(4\overline{Z}))}$, leading from equation (9) to :

$$f(Z) = -\frac{i\Gamma(r)}{2\pi} ln\Big(Z - Z_v\Big) + \frac{i\Gamma(r)}{2\pi} ln\left(\frac{D_b^2}{4Z} - \overline{Z_v}\right) + iU_z(r)\left(Z - \frac{D_b^2}{4Z}\right). \tag{10}$$

Then the velocities u and v, respectively in X- and Y-directions read :

$$u = \frac{\partial\Phi}{\partial X} = \frac{\partial\Psi}{\partial Y} \;\; ; \;\; v = \frac{\partial\Phi}{\partial Y} = -\frac{\partial\Psi}{\partial X}. \tag{11}$$

After using the unsteady Bernoulli theorem, the pressure within the fluid can be deduced for each two-dimensional section :

$$p(Z) + \frac{1}{2}\rho_0 U^2 + \rho_0\frac{\partial\Phi}{\partial t} = \left[p(Z) + \frac{1}{2}\rho_0 U^2 + \rho_0\frac{\partial\Phi}{\partial t}\right]_{|Z|\longrightarrow\infty}, \tag{12}$$

with $U^2 = u^2 + v^2$. Evaluating the pressure, the velocity and the time derivative of the velocity potential to the infinity downstream, the equation (12) leads to :

$$p(Z) + \frac{1}{2}\rho_0 U^2 + \rho_0\frac{\partial\Phi}{\partial t} = p_\infty + \frac{1}{2}\rho_0 U_z(r)^2 + \rho_0\Re\left(\frac{i\Gamma(r)\Omega r}{2\pi\overline{Z_v}}\right). \tag{13}$$

The pressure within the fluid is then deduced from (13) :

$$p(Z) - p_\infty = \frac{1}{2}\rho_0(U_z(r)^2 - U^2) + \frac{\rho_0\Gamma(r)\Omega r}{2\pi}\Re\left(\frac{i}{\overline{Z_v}} + \frac{i}{Z_v - Z} - \frac{i}{\overline{Z_v} - \frac{D_b^2}{4Z}}\right). \tag{14}$$

From the pressure within the fluid, the wall pressure on the surface of the cylinder is extracted taking $Z = D_b e^{i\theta_b}/2$. By projections on the X- and Y-axes (corresponding to the ϕ- and z-directions in the three-dimensional problem), the

forces per unit length exerted by the fluid on the cylinder in the tangential and axial directions for one blade passage are found as:

$$\hat{F}_{beam,\phi}(r,t) = \frac{D_b}{2}\int_0^{2\pi} p\left(\frac{D_b}{2}e^{i\theta_b}\right)\cos(\theta_b)d\theta_b \;\; ; \;\; \hat{F}_{beam,z}(r,t) = \frac{D_b}{2}\int_0^{2\pi} p\left(\frac{D_b}{2}e^{i\theta_b}\right)\sin(\theta_b)d\theta_b. \quad (15)$$

The rotor blades modeled by the vortex pass near the beam with a time period $2\pi/(B\Omega)$. The contributions of individual vortices can be summed if and only if they are separated by a large distance, thus if the rotor solidity is small. Since our investigations focus on a two-bladed rotor (see Tab. 1), this approximation is relevant. In the following, as the expressions for the axial and tangential forces are similar, only the expressions of the tangential force are developed :

$$F_{beam,\phi}(r,t) = \sum_{n=-\infty}^{\infty} \hat{F}_{beam,\phi}\left(r, t+\frac{2\pi}{B\Omega}n\right) = \sum_{k=-\infty}^{\infty} F^{(k)}_{beam,\phi}(r)e^{-ikB\Omega t}, \quad (16)$$

where :

$$F^{(k)}_{beam,\phi}(r) = \frac{B\Omega}{2\pi}\int_{-\infty}^{\infty} F_{beam,\phi}(r,t)e^{ikB\Omega t}dt. \quad (17)$$

Finally, these expressions are used to compute the sound pressure in the farfield generated by fluctuating loads on the beam with equation (8).

C. Model Inputs

This section gives an overview of the parameters and inputs used for the analytical modeling. The rotor and beam characteristics are the ones of the experimental campaign carried out by Gojon et al. [3]. The two-bladed rotor features a NACA0012 blade profile, of constant pitch. The rotor and beam dimensions are detailed in Table 1.

Parameters	
Number of blades B	2
Rotor angular speed Ω	837.8 rad/s
Tip-radius $r_{tip} = D/2$	0.1 m
Root-radius r_{root}	0.016 m
Blade pitch angle α	10°
Blade chord c	0.025 m
Beam diameter D_b	0.02 m
Beam axis-rotor plane distance L	0.02 m
Source-observer distance R	1.62 m
Air density ρ_0	1.20 kg/m^3
Sound speed c_0	340 m/s

Table 1 Geometric parameters and inputs for the analytical models.

The axial velocity profiles in the wakes of the rotor are presented in Fig. 5. These profiles are obtained from numerical simulation (grey and black lines) and from measurements (black circles). Numerically, an implicit large eddy simulation (iLES) is performed with the CFD commercial software Fluent v2020 R1, for the two-bladed rotor alone, without beam downstream. The computational domain is split into two volumes : an inner rotating volume including the rotor, and an outer static volume for the mast and the farfield boundary conditions. The flow is considered incompressible. The numerical setup is described in more detail by Gojon et al. [2]. Instantaneous axial velocity profiles (grey lines) and time-averaged over 360° (black lines) are obtained numerically at different axial positions z/r_{tip}, the rotor disk plane being at $z/r_{tip} = 0$. Experimentally, particle image velocimetry (PIV) measurements were carried out for the two-bladed rotor alone, in the ISAE SUPAERO anechoic room. PIV measurements were performed in the vertical plane containing the rotor axis. These experimental results (black circles) are in good agreement with

numerical results (the comparison is possible for $z/r_{tip} \leq -0.25$ only, due to the PIV setup, see Fig. 5a). Dispersion of instantaneous velocity profiles indicate fluctuations near the rotor disk plane, especially near the blade tip region (around $r/r_{tip} = 0.8$). These fluctuations may be caused by the flow separation and the resulting unsteadiness that occur in this region, as suggested by Jardin et al. [15]. Near the rotor disk plane, the axial velocity U_z induced by the rotor is maximum between $r/r_{tip} = 0.8$ and 0.9, and it drops at the very blade tip. This maximum is shifted and decreases when moving away from the rotor disk plane. This is associated with a relatively strong tip-vortex delimiting the rotor wake that contracts as it is advected downstream of the rotor, in line with momentum theory (also known as the vena contracta phenomenon). In Fig. 5b, the axial velocity profile interpolated from numerical results, at $z/r_{tip} = -0.1$ is presented. This velocity profile is used as an input in both models as it corresponds to the top part of the cylindrical beam.

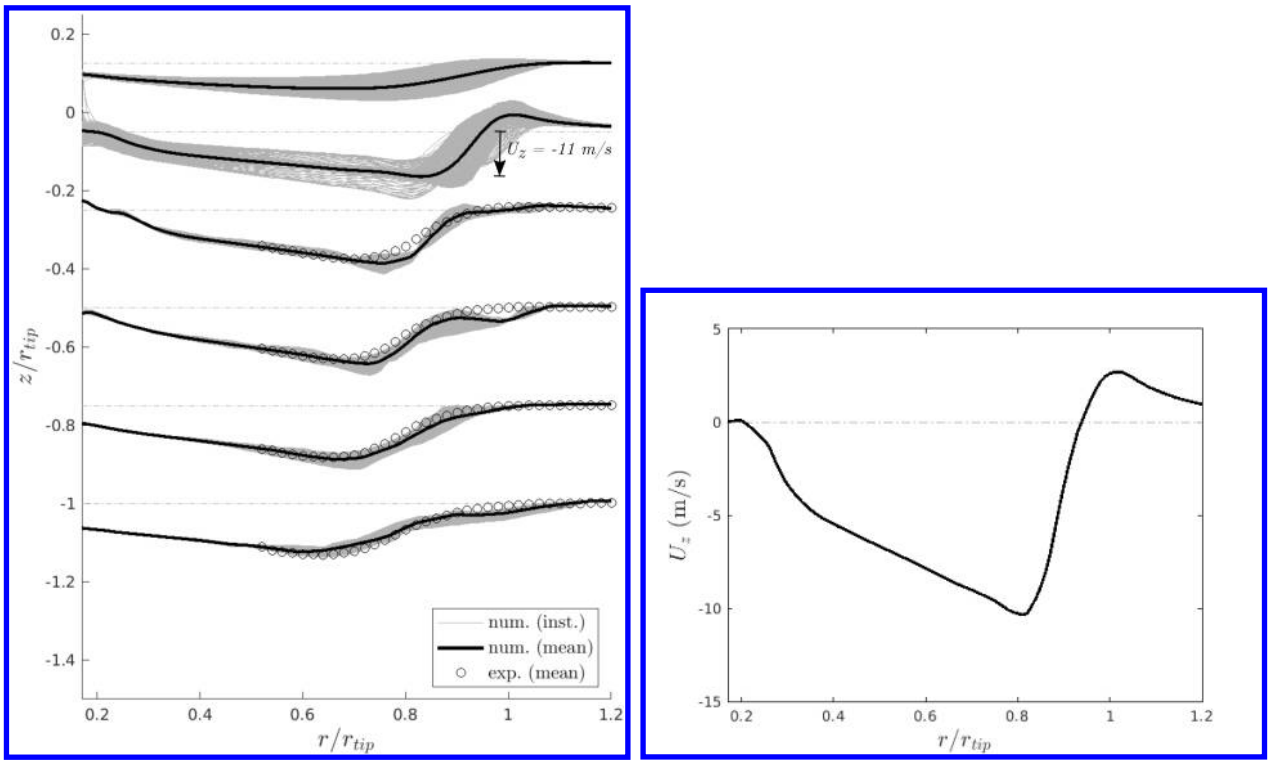

(a) Axial velocity profiles at various axial positions z/r_{tip} **(b) Interpolated axial velocity profile for $z/r_{tip} = -0.1$**

Fig. 5 Instantaneous (grey) and time-averaged (black) axial velocity profiles induced by the rotor without beam downstream, at 8000 RPM and at different axial positions z/r_{tip}, obtained by numerical simulations (iLES) and measurements (PIV).

The thrust distribution and the tangential force distribution of the two-bladed rotor are presented in Fig. 6. Instantaneous (grey lines) and time-averaged (black line) thrust and tangential force distributions are obtained from the iLES computation, without the beam (same simulation parameters as for the velocity profiles). One rotor blade is divided into 20 radial cross-sections, with a span-wise $dr/r_{tip} = 0.03$. The resulting axial and tangential forces of each cross-section are computed by summing the contributions of all mesh cells of the section. The instantaneous deviations with respect to the time-averaged distribution are negligible, except near the blade tip region, for $r/r_{tip} > 0.8$. As for the velocity profiles, it is probably caused by the flow separation and the resulting unsteady nature of the flow in this region.

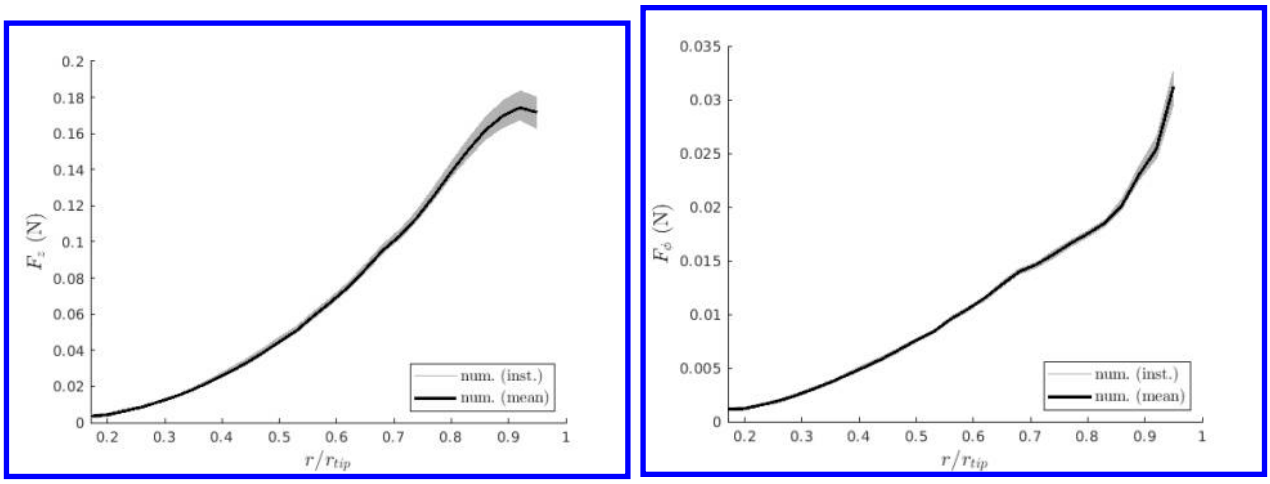

(a) Thrust distribution **(b) Tangential force distribution**

Fig. 6 Instantaneous (grey) and time-averaged (black) thrust and tangential force distributions of the two-bladed rotor without beam downstream, at 8000 RPM, obtained by numerical simulations (iLES).

V. Acoustic Results

In this section, the acoustic results are presented. The farfield spectra are first reported and analyzed, followed by three dimensional directivity diagrams. Results obtained with the analytical models are compared to results from experiments and numerical simulations, previously presented by Gojon et al. [2], [3]. For the numerical simulation, the Ffowcs Williams and Hawkins (FW-H) analogy is applied to propagate the fluctuating pressure of different acoustic surface sources in the farfield. Then, for both numerical simulation and experiment, the acoustic spectra are obtained from time signals by computing the fast Fourier transform (FFT) with a Hanning window applied, respectively, on 2 and 100 samples, using a 60% and 50% overlap and an amplitude correction factor. The frequency resolution is the same for both numerical and experimental results, and is equal to $\Delta f = 3.125$ Hz.

A. Farfield Spectra

The sound pressure level (SPL) spectra measured (black line) at a source-observer distance $R = 1.62$ m, are reported in Fig. 7, for various observer positions : $\phi_{exp} = 90°$ and $0°$, $\theta_{exp} = 0°$ and $-40°$. Tonal noise at the blade passing frequency (BPF), i.e. at 266 Hz, and its harmonics is clearly identified, as well as tones at multiples of the rotational frequency. The latter are most likely caused by mechanical imbalance. Tone levels extracted from numerical spectra (red circles) and tone levels directly computed with the models (blue squares) are also reported. The observer position considered for each spectrum is depicted using the black dot on the inset of each figure. Fig. 7 presents the total noise, i.e. the noise radiated by both rotor blades and beam in the farfield. The thickness noise model (not detailed here, see Hanson's work [10]), the steady and unsteady blade loading noise model (detailed in IV.A) and the unsteady beam loading noise model (detailed in IV.B) are summed to obtain the total noise model. Figure 7 shows a very good overall agreement between the model, the measured spectra and the numerical results. For an observer position in the rotor disk plane ($\theta_{exp} = 0°$), harmonic levels are highly dependent on the azimuthal position of the observer ϕ_{exp}. Fig. 7a shows important harmonic levels for $\phi_{exp} = 90°$, $\theta_{exp} = 0°$ (in the direction normal to the beam), except at 2×BPF where there is a drop before further increase at 3×BPF, leading to a hump of harmonics centered around 5×BPF. The envelope of the hump is highlighted by black (experiments), red (numerical simulations) dashed lines, and blue dotted lines (model). Conversely, Fig. 7b reports very low harmonic levels for $\phi_{exp} = 0°$, $\theta_{exp} = 0°$ (on the beam axis). A minimum SPL is observed at 3×BPF. This minimum is not clearly captured by the model or with numerical simulations. At the BPF, the SPL is very similar in both spectra (Fig. 7a and 7b). Fig. 7c and 7d report qualitatively the same hump of harmonics for an observer position downstream of the rotor disk plane ($\theta_{exp} = -40°$). However, we note that some measured harmonic levels are not well predicted by the model and the numerical simulations. At the BPF, the SPL from experiments is recovered by the model and the numerical simulations for $\phi_{exp} = 90°$, $\theta_{exp} = -40°$. However, it is overestimated by the model and underestimated by numerical simulations for $\phi_{exp} = 0°$, $\theta_{exp} = -40°$.

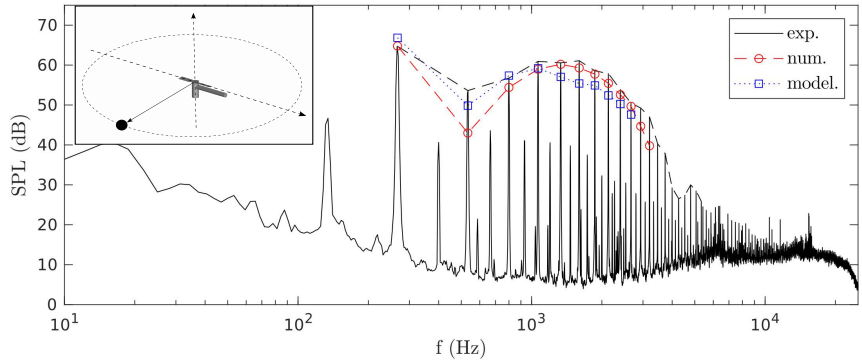

(a) $\phi_{exp} = 90°$ **;** $\theta_{exp} = 0°$

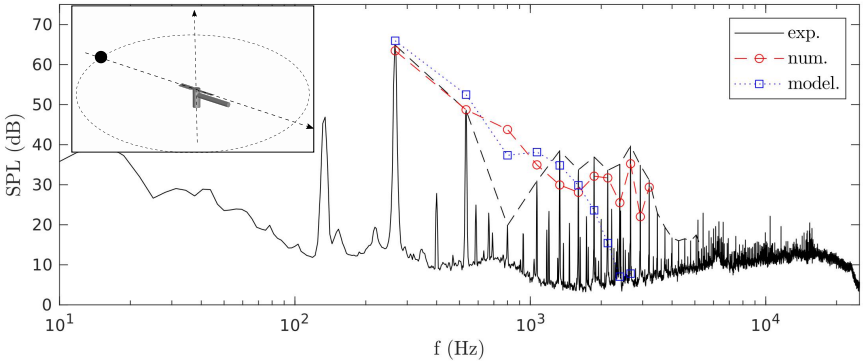

(b) $\phi_{exp} = 0°$ **;** $\theta_{exp} = 0°$

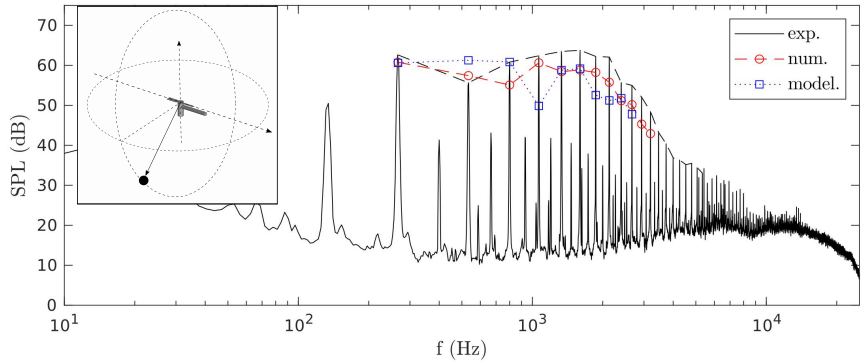

(c) $\phi_{exp} = 90°$ **;** $\theta_{exp} = -40°$

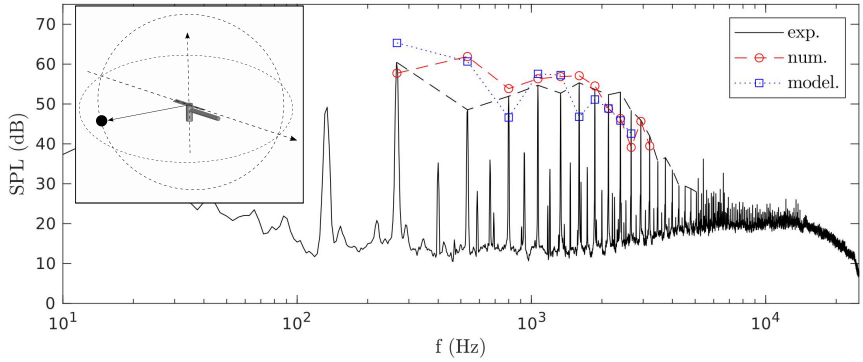

(d) $\phi_{exp} = 0°$ **;** $\theta_{exp} = -40°$

Fig. 7 Sound pressure level (SPL) spectra and tone levels at different observer positions : $\phi_{exp} = 90°$ **and** $0°$**,** $\theta_{exp} = 0°$ **and** $-40°$**. Results from experiments and numerical simulations are compared to the model.**

Figure 8 presents rotor (red) and beam (blue) noise contributions obtained with numerical simulations (circles) or with the model (squares), for two observer positions in the rotor disk plane : $\phi_{exp} = 90°$ (normal to the beam) and $\phi_{exp} = 0°$ (on the beam axis). The rotor noise (red squares) is the sum of thickness noise, steady-loading noise and unsteady-loading noise. It is found in very good agreement with the numerical simulations (red circles), only considering the rotor sources. The beam noise (blue squares) corresponds to the unsteady beam loading noise model. It is in a very good agreement with numerical simulations (blue circles), in which only the beam sources are taken into account. In Fig. 8a, for $\phi_{exp} = 90°$, the rotor noise contribution is dominant at the BPF, while for the BPF harmonics, the beam noise is the main contributor. The hump of harmonics centered around 5×BPF is well reproduced. In Fig. 8b, for $\phi_{exp} = 0°$, the rotor noise contribution is dominant at the BPF and its harmonics. The noise radiated by the beam is very low.

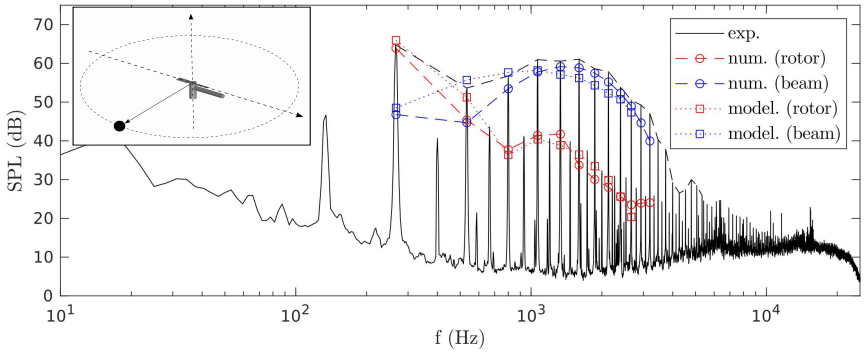

(a) $\phi_{exp} = 90°$ **;** $\theta_{exp} = 0°$

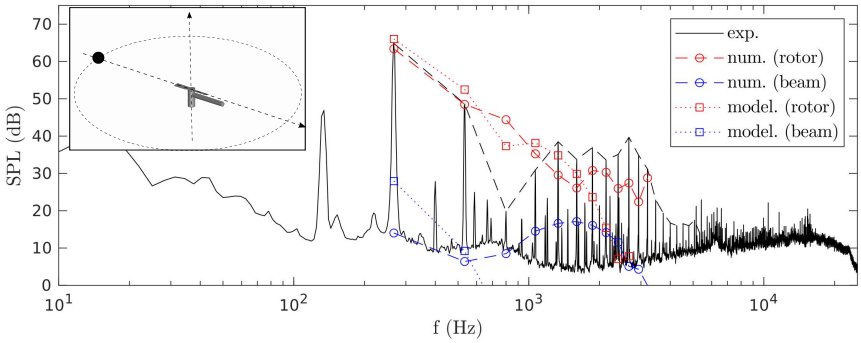

(b) $\phi_{exp} = 0°$ **;** $\theta_{exp} = 0°$

Fig. 8 Sound pressure level (SPL) spectra and tone levels at different observer positions : $\phi_{exp} = 90°$ **and** $0°$**,** $\theta_{exp} = 0°$**. Rotor and beam contributions from numerical simulations are compared to the model.**

To summarize, the rotor noise contribution is dominant at the BPF, independently of the observer position. Yet the resulting level depends on the observer position. The thickness noise and the steady loading noise radiated by the blades are known to be dominant at the BPF, with a maximum level in directions close to the rotor disk plane. This explains the lower BPF level for an observer position off this plane. At the BPF harmonics, the unsteady-loading noise radiated by the blades and the beam is the main contributor. By separating the contributions of the rotor and of the beam in Fig. 8, the difference in the hump of harmonics between Fig. 7a and Fig. 7b can be explained. The unsteady-loading noise on the beam radiate in directions normal to its surface, i.e. with no contribution along the beam axis. This explains the high harmonic levels observed in Fig. 7a. The rotor unsteady-loading noise radiates in directions normal to the blade chord, with a minimum around the rotor disk plane. This explains the low harmonic levels observed in Fig. 7b, corresponding to an observer position on the beam axis, nearly in the rotor disk plane. The three-dimensional directivity patterns presented in the next section will help explaining in more details these level differences.

B. Directivity Patterns

Fig. 9 presents the 3D directivities of the total noise radiated by the rotor-beam configuration in the farfield, at the BPF, 4×BPF and 5×BPF. Experimental 3D directivities are not complete since the arc antenna of microphones is from $\theta_{exp} = -60°$ to $\theta_{exp} = 60°$. No acoustic measurement is available for high latitude angles. The rotor disk plane is represented by the dashed circle and the beam by the thick black line. The 3D noise directivities obtained with the model are in good agreement with the experimental and numerical directivities. The BPF directivities (Fig. 9a, 9b and 9c) show a monopole-like pattern with a maximum level in the rotor disk plane. These BPF directivities are in agreement with the BPF levels analyzed in the previous section. Two minima are also visible on the upper part of the sphere, for results from numerical simulations and from the model (Fig. 9b and 9c). Two other minima are present on the lower part (not visible). The 4×BPF directivities (Fig. 9d, 9e and 9f) show a dipole-like pattern with minima on the beam axis. Furthermore, Fig. 9e and 9f exhibit an asymmetry with respect to the rotor disk plane, with a lower level downstream of the rotor, in the plane normal to the beam axis. The 5×BPF directivities (Fig. 9g, 9h and 9i) show a similar dipole-like pattern with same minima on the beam axis. Fig. 9g and 9h are very similar and symmetric with respect to the rotor disk plane. In contrast, Fig. 9i features asymmetry between the upper part and the lower part of the 3D pattern. Yet, the harmonic directivities globally corroborate the observations of the previous section, on the farfield spectra and harmonic levels.

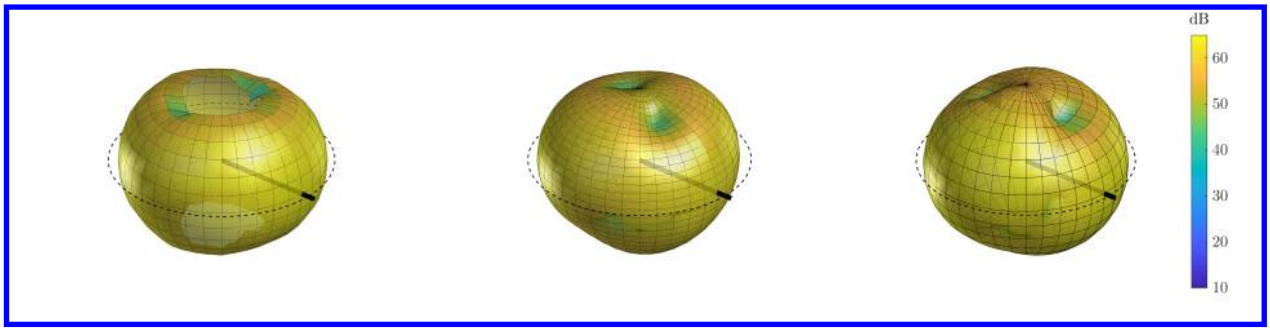

(a) BPF - Exp. **(b) BPF - Num.** **(c) BPF - Model**

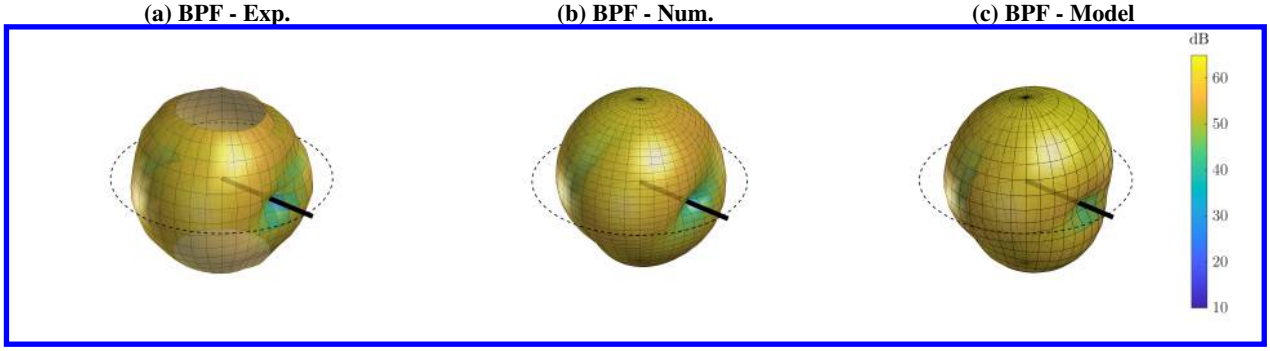

(d) 4×BPF - Exp. **(e) 4×BPF - Num.** **(f) 4×BPF - Model**

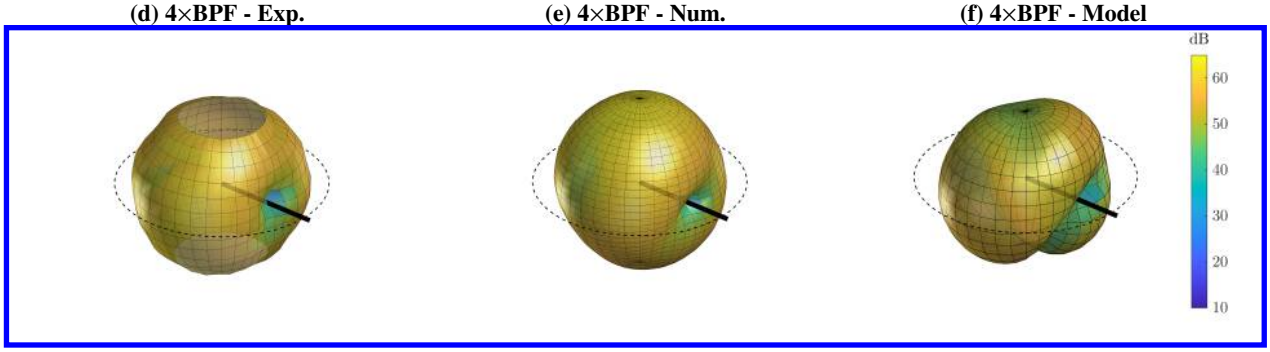

(g) 5×BPF - Exp. **(h) 5×BPF - Num.** **(i) 5×BPF - Model**

Fig. 9 3D total noise directivities of the two-bladed rotor with the cylindrical beam downstream, at BPF, 4×BPF and 5×BPF. Results from experiments and numerical simulations are compared to the model.

Figure 10 reports the 3D directivities radiated by the rotor blades or the beam in the farfield, at 5×BPF. Directivities obtained with the model are compared to those obtained from numerical simulations. The rotor noise directivities (Fig. 10a and 10b) show a dipole-like pattern with a minimum over all the rotor disk plane. Looking closer, the dipole-like pattern obtained with the model is tilted. This tilt angle is due to the pitch angle of the rotor blades, as the maximum level is in the direction normal to the blade chord. The difference in noise directivity noticed in Fig. 9h and 9i, between the model and numerical results, can probably be explained by the tilted directivity of the unsteady blade loading noise model, compared to the almost non-tilted rotor noise directivity obtained with the numerical simulation. This difference in the 3D directivity patterns need further investigations. The beam noise directivities (Fig. 10c and 10d) show a dipole-like pattern with minima aligned with the beam axis.

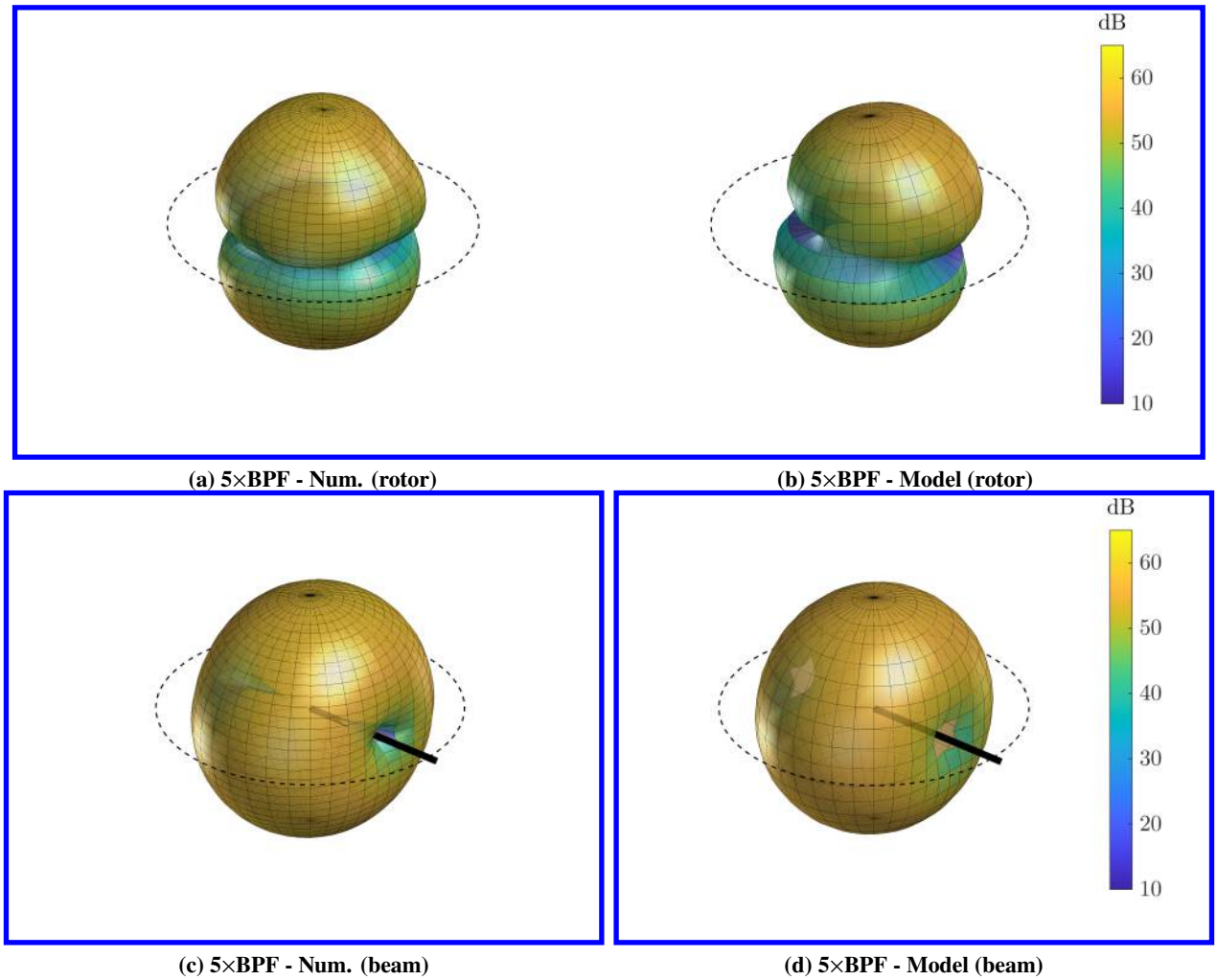

(a) 5×BPF - Num. (rotor) **(b) 5×BPF - Model (rotor)**

(c) 5×BPF - Num. (beam) **(d) 5×BPF - Model (beam)**

Fig. 10 3D noise directivities of the two-bladed rotor with the cylindrical beam downstream at 5×BPF. Rotor and beam contributions from numerical simulations are compared to the model.

VI. Conclusion

This paper described two analytical models, aimed at clarifying the aeroacoustic mechanisms involved in a rotor-beam configuration. The latter is typical of small-size UAVs, for which rotors are connected to the main structure with a beam. Various competing sources are assessed in this paper, namely thickness noise, steady-loading and unsteady-loading blade noise, and beam unsteady-loading noise. Simple uncoupled models, developed for the unsteady-loading noise contributions, were detailed. The first model determines fluctuating forces on the blades, caused by a stationary azimuthal flow distortion, due to the presence of the beam downstream. The second model predicts the fluctuating forces

on the beam, due to the circulation of the passing blades. Tone levels, as well as three dimensional noise directivity patterns, obtained with the models are in very good agreement with the experimental and numerical results. At the BPF, a 'flattened' monopole-like pattern is recovered with the model, with maxima in the rotor disk plane. This is explained by an important contribution of the thickness noise and the steady-loading noise radiated by the rotor. At the BPF harmonics, the hump noticed by Gojon et al. [2] is recovered with the model. The beam noise contribution is significant in the rotor disk plane, with maxima in directions normal to the beam, and minima on the beam axis, while the rotor noise contribution is maximal in the direction normal to the blade chord. This behaviour is clearly identified in the 3D directivity patterns, where the unsteady beam loading noise gives a dipole-like pattern with minima on the beam axis, and the unsteady blade loading noise gives a tilted dipole-like pattern with a minimum level over all the rotor disk plane. Therefore, even if the model has its own limitations (approximations, quasi-two-dimensional formulation), and if some aeroacoustic mechanisms have not been assessed yet (tip-vortex impingement on the beam, or sound scattering), it allows to obtain good qualitative and quantitative acoustic results, cross-validated with simulations and experiments on the same configuration.

Acknowledgments

The authors acknowledge with gratitude financial support from the DGA. They are grateful to the entire ISAE-SUPAERO technical team for the success of the experimental campaign. The numerical part of this work was performed using resources from GENCI [CCRT-CINES-IDRIS] (Grant 2023-[A0142A07178]).

References

[1] Zawodny, N. S., and Boyd, D. D., "Investigation of rotor–airframe interaction noise associated with small-scale rotary-wing unmanned aircraft systems," Journal of the American Helicopter Society, Vol. 65, 2017.

[2] Gojon, R., Doué, N., Parisot-Dupuis, H., Mellot, B., and Jardin, T., "Aeroacoustic radiation of a low Reynolds number two-bladed rotor in interaction with a cylindrical beam," Proceedings of the 28th AIAA/CEAS Aeroacoustics 2022 Conference, 2022, p. 2972.

[3] Gojon, R., Parisot-Dupuis, H., Mellot, B., and Jardin, T., "Aeroacoustic radiation of low Reynolds number rotors in interaction with beams," The Journal of the Acoustical Society of America, Vol. 154, 2023, pp. 1248–1260.

[4] Doué, N., Gojon, R., and Jardin, T., "Numerical investigation of the acoustics radiation of a two-bladed rotor in interaction with a beam," The 6th Symposium on Fluid-Structure-Sound Interactions and Control, 2023.

[5] Brand, A. G., MacMahon, H. M., and Komerath, N. M., "Surface Pressure Measurements on a Body Subject to Vortex Wake Interaction," AIAA Journal, Vol. 27, No. 5, 1989.

[6] Affes, H., and Conlisk, A. T., "Model of Rotor Tip Vortex-Airframe Interaction, Part I: Theory," AIAA Journal, Vol. 31, No. 12, 1993.

[7] Affes, H., Conlisk, A. T., Kim, J. M., and Komerath, M., "Model of Rotor Tip Vortex-Airframe Interaction, Part II: Comparison with Experiment," AIAA Journal, Vol. 31, No. 12, 1993.

[8] Roger, M., Vella, E., Rendon, J., Moreau, S., and Pereira, A., "Aerodynamic and Sound-Scattering Effects in Rotor-Strut Interaction Noise of Small-Size Drones," AIAA Aviation and Aeronautics Forum and Exposition, 2023.

[9] Wu, Y., Kingan, M., and Go, S., "Propeller-strut interaction tone noise," Physics of Fluids, Vol. 34, 2022.

[10] Hanson, D. B., and Parzych, D. J., "Theory for Noise of Propellers in Angular Inflow With Parametric Studies and Experimental Verification," NASA Contractor Report 4499, 1993.

[11] Sears, W. R., "Some Aspects of Non-Stationary Airfoil Theory and Its Practical Application," Journal of The Aeronautical Sciences, 1940.

[12] Roger, M., Moreau, S., and Guédel, A., "Vortex-shedding noise and potential-interaction noise modeling by a reversed sears," 12th AIAA/CEAS Aeroacoustics Conference, 2006.

[13] Parry, A. B., "Theoritical Prediction of Counter-Rotating Propeller Noise," PhD Thesis, 1988.

[14] Lowson, M. V., "Theoritical Studies of Compressor Noise," NASA Contractor Report 1287, 1969.

[15] Jardin, T., Gojon, R., Doué, N., and Parisot-Dupuis, H., "Numerical and experimental analysis of the influence of solidity on rotor aeroacoustics at low Reynolds numbers," International Journal of Aeroacoustics, Vol. 0, 2022, pp. 1–25.